This article has been accepted for publication in a future issue of this journal, but has not been fully edited. Content may change prior to final publication. Citation information: DOI 10.1109/TDMR.2016.2597740, IEEE Transactions on Device and Materials Reliability

Micro-Structural Indicators for Assessment of Effect of Prolonged and Intermittent Storage on Reliability of Leadfree Electronics

Pradeep Lall, *Fellow, IEEE*, Kazi Mirza, Mahendra Harsha, Kai Goebel

***Abstract*— Electronic systems may be subjected to prolonged and intermittent periods of storage prior to deployment or usage. Prior studies have shown that leadfree solder interconnects show measurable degradation in the mechanical properties even after brief exposures to high temperature. In this paper, a method has been developed for determining equivalent storage time to produce identical damage at a different temperature. Electronics subjected to accelerated tests often have a well-defined thermal profile for a specified period of time. Quantification of the thermal profile in field deployed electronics may be often difficult because of variance in the environment conditions and usage profile. There is need for tools and techniques to quantify damage in deployed systems in absence of macro-indicators of damage without knowledge of prior stress history. Approach for mapping damage in leadfree second-level interconnects between different thermal conditions is new. High reliability applications such as avionics and missile systems may be often exposed to long periods of storage prior to deployment. Effect of storage at different temperature conditions can be mapped using the presented approach. A framework has been developed to investigate the system state and estimate the remaining useful life of solder ball subjected to a variety of isothermal aging conditions including 60°C, 75°C and 125°C for periods of time between 1-week and 4-week. Data on damage precursors including rate of change in normalized phase growth and normalized IMC thickness has been collected and analyzed to derive physics based damage mapping relationships for aging. Mathematical relationships have been derived for the damage mapping to various thermal storage environments to facilitate determining appropriate time-temperature combination to reach a particular level of damage state. Activation energy for the leading indicators of failure is also computed. Specific damage proxies examined include the phase-growth indicator and the intermetallic thickness. The viability of the approach has been demonstrated for leadfree test assemblies subjected to multiple thermal aging at 60° C, 75°C and 125°C. Damage mapping relationships are derived from data based on the two separate leading indicators.**

***Index Terms*—Materials Reliability, Integrated Circuit Reliability, Soldering, Integrated Circuit Interconnections.**

I. INTRODUCTION

LEADFREE electronics in automotive, military and defense applications may be subjected to extreme high and extreme low temperature in addition to temperature cycling with intermittent prolonged period of storage. Automotive electronics may be expected to last 10-years, 100,000 miles. Military and defense electronics may be subjected to several deployments over the use-life of the system. Previous researchers have shown the detrimental effects of prolonged exposure to high temperature on the mechanical properties of lead-free alloys. Effects include the degradation in the yield strength and ultimate tensile strength of the materials. [Chou 2002, Hasegawa 2001, Zhang 2009]. The effects are most pronounced in the widely used SnAgCu based alloys including SAC105, SAC205, SAC305 and SAC405 solders. Lower silver solders such as the SAC105, often touted for their resistance to transient dynamic shock and vibration, are the most susceptible to thermal aging amongst the SAC solders. The effects have been verified in the solder alloys at both lower strain rates in the neighborhood of 10^{-4} sec^{-1} to 10^{-5} sec^{-1} typical of thermal cycling, and at 1-to-100 sec^{-1} typical of shock and vibration. Degradation in the neighborhood of 50% has been measured at low temperature exposures.

The property evolution of the SnAgCu solder alloys poses a challenge in the long life systems in presence of multiple redeployments over the product life. Electronics in automotive systems may perform critical functions such as collision avoidance, lane departure warning, adaptive cruise

Manuscript received November 27, 2014. The research results presented in this paper are based on projects supported by industrial members of the NSF-CAVE3 Electronics Research Center at Auburn University.

Pradeep Lall is MacFarlane Endowed Professor and Director with the Auburn University, Auburn, AL 36849, USA (corresponding author to provide phone: 334-844-3424; fax: 334-844-3450; e-mail: lall@auburn.edu).

Kazi Mirza is Graduate Research Assistant with Auburn University, Department of Mechanical Engineering, Auburn, AL 36849, USA (e-mail: kmm0039@tigermail.auburn.edu).

Mahendra Harsha was previously a Graduate Research Assistant with Auburn University, Department of Mechanical Engineering, Auburn, AL 36849. He is presently with Skyworks, Inc. (e-mail: mahendra.harsha@skyworksinc.com).

Kai Goebel is with NASA Ames Research Center, Moffett Field, CA 94035-1000 (e-mail: kai.f.goebel@nasa.gov).

control, and antilock braking. Aerospace electronics systems may be called on to perform a variety of function including launch, autonomous navigation, in-flight maneuvering, path correction and re-entry. Long-life systems often may see multiple deployments during usage. The level-of-damage and the remaining useful life often need to be quantified in safety critical functions of long-life systems prior to subsequent re-deployment. Built-in self-test (BIST) is used to diagnose errors and detect malfunction with little or no interaction with external test equipment. Previous studies have shown that BIST can trigger false alarms resulting in pre-mature or unnecessary repair or replacement [Allen 2003, Drees 2004, Gao 2002, Rosenthal 1990]. Further, the BIST may provide only limited insight into the underlying damage state and the remaining useful life. Fuses and canaries are designed to fail prior to system failure due to a specific failure mode. Fuse failure provides advance warning and flag the damage state of the system. This advance warning is intended to provide a sufficient maintenance window to allow repair or replacement prior to catastrophic failure [Mishra 2002, Anderson 2004]. Quantification of damage state prior to fuse or canary failure is often difficult. Further, the correlation of fuse or canary to the remaining useful life is often challenging.

Leadfree solder property evolution has been shown to increase in magnitude with both increase in ambient temperature and increase in time of exposure. Given the mission critical nature of the role of electronics in such applications, there is need for tools and techniques which can be used for capturing the evolving failure threshold, and damage accrued after multiple exposures to arbitrary temperatures for unforeseen lengths of time. Capability to equivalence damage over various storage temperature and times is beyond the state of art. Previously, leading indicators of damage have been used to quantify the accrued thermo-mechanical damage under steady-state and cyclic temperature exposure in leadfree solders. [Lall 2011[a-b], 2012[a-b]]. In this paper, a method has been developed for calculation of equivalent damage in leadfree second level interconnects. Leadfree electronics packages have been subjected to isothermal exposure at 60°C, 75°C and 125°C for various lengths of time. A method has been developed to interrogate the damage state due to prolonged thermal storage in electronic systems with leadfree second level interconnects. Levenberg-Marquardt Algorithm has been used in conjunction with microstructural leading indicators of failure. A test case has been presented to validate the ability of the proposed technique to map damage between different thermal conditions. The ability to map damage has been used to accrue damage under varied thermal conditions encountered in field deployment to ascertain the level of damage and the remaining useful life of the system. The test case has been demonstrated on a CABGA256 test assembly which has been subjected to 168 hours of thermal aging at 125°C followed by 250 cycles of -40 to 125°C and 250 cycles of 0 to 100°C thermal excursions.

II. Test Vehicle

In this study, Chip-Array Ball Grid Arrays (CABGA) have been used for the test. Specifically, CABGA36 and CABGA 256 packages soldered to glass-epoxy laminate board assemblies were used. The CABGA36 package is 6mm x 6mm in size, with 36 I/O, at 0.8 mm Pitch. The CABGA256 package is 16mm x 16mm in size, with 256 I/O at 0.8mm Pitch. Package interconnects were made of Sn3Ag0.5Cu solder in both cases. The ball diameter of the solder interconnects is 0.46 mm for the CABGA36 and 0.5 mm for the CABGA256.

Table 1: Package Attributes

Attributes	CABGA 36	CABGA256
Solder	Sn3Ag0.5Cu	Sn3Ag0.5Cu
Package Size (mm)	6x6	16x16
Package Type	CABGA	CABGA
I/O Count	36	256
I/O Pitch (mm)	0.8	0.8
Ball Diameter (mm)	0.46	0.5
Mold thickness (mm)	1.5	1.5
Board Finish	ImAg	ImAg
PCB Thickness	1.55	1.55
PCB Pad	NSMD	NSMD
Package Pad	SMD	SMD
Package Finish	Electroless NiAu	Electroless NiAu

Figure 1: CABGA 36 Package

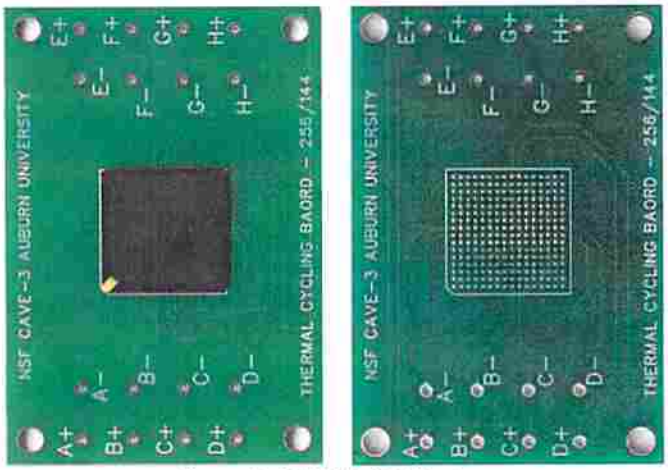

Figure 2: CABGA 256 Package

The printed circuit board thickness was 1.55 mm in both cases. Attributes of the test assembly package are shown in Table 1. Printed circuit board used in the test assembly was a double-sided FR4-06 material. The printed circuit board pads were non-solder mask defined (NSMD) with immersion silver finish. Figure 1 and Figure 2 shows the CABGA 36 and CABGA 256 package respectively and its array configuration.

All test vehicles were subjected to isothermal aging at 60°C, 75°C and 125°C for various lengths of time. The test board is a JEDEC form-factor test board with corner holes. Each test package has four daisy chain patterns corresponding to the four quadrants. Packages were assembled at in-house surface mount facility of CAVE3.

III. Approach for Interrogation of Damage in Thermal Aging Environments

In operational environments electronic systems may be stored after manufacture for a finite period prior to deployment. During the storage period, the systems may be exposed to a finite time-period of thermal aging at extreme low or extreme high temperatures in addition to thermal cycling. Once deployed, the systems may be exposed to further thermal aging along with intermittent thermo-mechanical cycling due to power on-off cycles or ambient temperature excursions. Extended exposure to elevated temperature aging may reduce thermo-mechanical reliability in cyclic environments. In this paper, a damage mapping method has been presented based on the underlying failure physics to relate the damage accrued under steady-state thermal aging with a particular combination of temperature and storage time. The approach has been developed in three steps.

A. Micro-structural Evolution of Damage

In this step, board assemblies have been subjected to single stresses of thermal aging. Samples have been withdrawn periodically and cross-sectioned. Damage proxies studied include the phase-growth parameter, rate of change of phase growth parameter per cycle and the intermetallic thickness. The phase-growth parameter is represented by symbol 'S' and defined in Equation (1). Previously, it has been shown that the rate of change in phase growth parameter [d(lnS)/d(lnN)] is valid damage proxy for prognostication of thermo-mechanical damage in solder interconnects and assessment of residual life [Lall 2011[a-b], 2012[a-b]] – where 'N' is the number of cycles. The damage proxy [d(lnS)/d(lnN)] is related to the micro structural evolution of damage by the following equation:

$$S = g^4 - g_0^4 = at^b \exp\left(\frac{-E_A}{K_B T}\right) \quad (1)$$

where, g is the average grain size at time of prognostication, g_0 is the average grain size of solder after reflow, t is the period of aging, S is the phase growth parameter, parameters a and b are the coefficient and exponent respectively. It is anticipated that, longer period of aging at higher temperature will result in higher accrued thermo-mechanical damage in a shorter time and result in a higher slope of the phase growth parameter versus time of aging curve. Test samples have been withdrawn and cross-sectioned at periodic intervals. Images of polished samples were taken under Optical Microscope at 750x-1000x magnification. . Growth rate of tin and Ag_3Sn phases was observed. Phase size is measured using image analysis software NI-MAQ. The quantitative measure of Ag_3Sn phase size was determined from a 480µm x 360µm rectangular region selected from the optical images. Figure 3 shows the mapping of image.

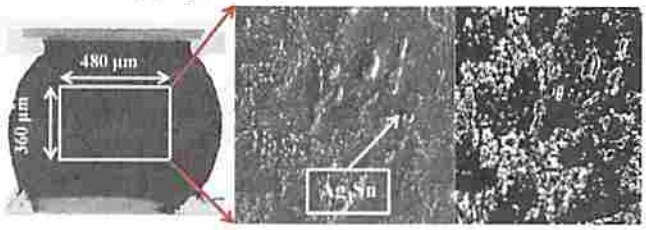

(a) (b) (c)

Figure 3: (a) Optical Micrograph of the solder joint after cross-sectioning (b) segmentation of the central rectangular region of size 360µm x 480µm (c) Gray scale mapping of image into black-and-white regions using image analysis software.

Growth of Inter-Metallic thickness during thermal aging has been studied as another leading indicator of failure in bulk solder. From past studies it has been established that growth of intermetallic thickness is used as a damage precursor for computation of remaining useful life [Lall 2011[a-b], 2012[a-b]]. The interfacial intermetallic layers are formed between solder and copper, and some precipitates appear near the interface of the IMCs/solder as shown in Figure 4. These intermetallic layers have been identified to consist of Cu_3Sn and Cu_6Sn_5 phases [Lall 2005]. Trend analysis of intermetallic thickness growth using image processing software, indicates that IMC thickness changes with the square root of aging time.

$$y(t) = y_0 + kt^n \exp\left(\frac{-E_A}{K_B T}\right) \quad (2)$$

where y(t) is IMC growth thickness during aging, y_0 is the initial thickness of intermetallic compounds, k is the coefficient standing for the square root of the diffusivity at aging temperature, t is aging time, E_A is the activation energy, K_B is Boltzmann's Constant (8.617 x 10^{-5} ev/K) and T_A is aging temperature in Kelvin . The exponent value, n = ½ has been used in the above equation, which reveals a diffusion-controlled mechanism during aging.

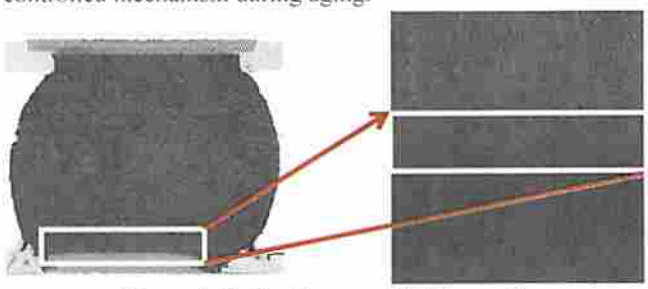

Figure 4: Optical Image of IMC growth

B. Damage Mapping Relationships for Phase Growth

The relation between phase growth and aging time has been normalized with respect to the initial phase size, as follows.

$$S_n = \left(\frac{g_p}{g_0}\right)^4 - 1 = a_0 t^{b_0} \quad (3)$$

$$= a_1 \exp\left(\frac{-E_A}{K_B T}\right)\left[t^{b_1 \exp\left(-E_B / K_B T\right)}\right]$$

Where S_n is the normalized phase growth parameter, 'a_1' is the coefficient for phase growth, 'b' is the phase-growth exponent, E_A is the activation energy, K_B is the Boltzmann Constant, T is the temperature in Kelvin. The normalized phase growth expression has been rearranged as follows:

$$S_n = a_0 t^{b_0} \quad (4)$$

$$\ln S_n = \ln a_0 + b_0 \ln t \quad (5)$$

Where, (6)

$$a_0 = a_1 \exp\left(\frac{-E_A}{K_B T}\right)$$

Taking a natural logarithm of Equation (6), the relationship has been reduced to that of a straight line, where a'_1 is the temperature dependent phase-growth coefficient. From Equation (6) we can write:

$$\ln(a_0) = \ln(a_1) - \left(\frac{E_A}{K_B T}\right) \quad (7)$$

By using equation (3) and (7) the relationship between aging temperature (T) and aging time (t) for a particular level of damage state in terms of phase growth has been computed. The activation energy of the exponent term has been computed by fitting the phase growth data to the following form of the equation:

$$b_0 = b_1 \exp\left(\frac{-E_B}{K_B T}\right) \quad (8)$$

Taking a natural logarithm of Equation (6), the relationship has been reduced to that of a straight line, where b_1 is the temperature dependent phase-growth coefficient. From Equation (6) we can write:

$$\ln(b_0) = \ln(b_1) - \left(\frac{E_B}{K_B T}\right) \quad (9)$$

Where b_0 is the temperature dependent phase-growth exponent, E_B is the activation energy, K_B is the Boltzmann Constant, T is the temperature in Kelvin.

C. Damage Mapping Relationships for IMC Growth

The intermetallic thickness based proxy has been related to aging temperature and aging time using the following normalized IMC thickness equation.

$$Y_n = \frac{y_p}{y_0} - 1 = k_0 t^{0.5} = k_1 t^{0.5} \exp\left(\frac{-E_A}{K_B T}\right) \quad (10)$$

$$Y_n = k_0 \sqrt{t} \quad (11)$$

$$\ln Y_n = \ln k_0 + \frac{1}{2} \ln t \quad (12)$$

Where, (13)

$$k_0 = k_1 \exp\left(\frac{-E_A}{K_B T}\right)$$

Taking a natural logarithm of Equation (13), the relationship has been reduced to that of a straight line, where k_0 is the temperature dependent IMC-growth coefficient. From Equation (13) we can write:

$$\ln(k_0) = \ln(k_1) - \left(\frac{E_A}{K_B T}\right) \quad (14)$$

By using equation (10) and (14) a relation between aging temperature (T) and aging time (t) for a particular level of damage state in terms of IMC thickness has been derived. Convergence between the damage mapping relationships has been studied to validate the damage equivalency.

IV. Leading Indicators for Thermal Aging

A set of packages was subjected to aging at 60°C, 75°C and 125°C and were withdrawn after a periodic time-interval of 1-week or 168-hours. Each of the samples was cross-sectioned, polished and imaged using an optical microscope. The same joint was examined in each cross-section. Phase growth and intermetallic growth was studied using images taken by Optical microscope at each time interval.

A. Phase-Growth Damage Proxy

The image analysis software has been used to measure the average phase size. Equation (3) represents the evolution of phase growth in thermal aging based on experimental data. The test data has been used to derive the parameters for normalized phase growth of Equation (3). Micrographs of phase structure are shown in Figure 5 for CABGA36 at 60°C, and in Figure 6 for CABGA36 at 60°C.

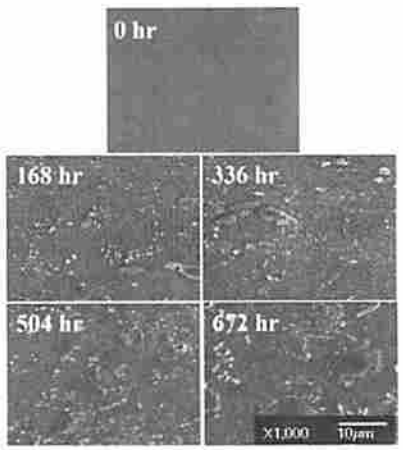

Figure 5: Optical Microscopic images of Phase Growth in CABGA36 at different time intervals at 60°C

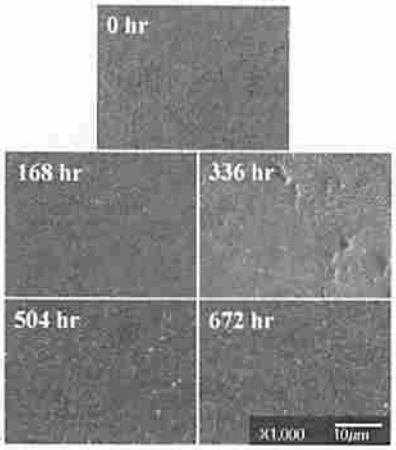

Figure 6: Optical Microscopic images of Phase Growth in CABGA256 at different time intervals at 60°C

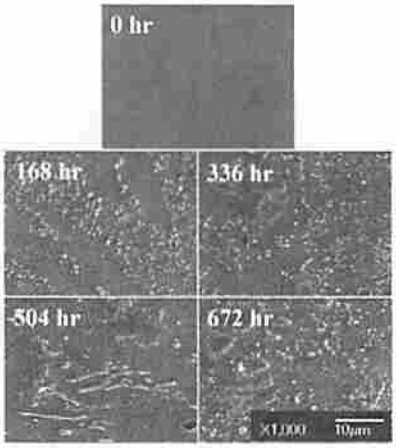

Figure 7: Optical Microscopic images of Phase Growth in CABGA36 at different time intervals at 75°C

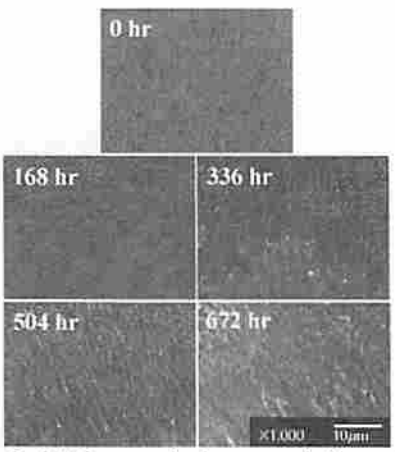

Figure 8: Optical Microscopic images of Phase Growth in CABGA256 at different time intervals at 75°C

Micrographs of phase structure are shown in Figure 7 for CABGA36 at 75°C, and Figure 8 for CABGA256 at 75°C. Figure 9 shows the micrographs for CABGA36 at 125°C and Figure 10 shows the micrographs for CABGA 256 packages at 125°C. All the micrographs have been captured at a time-interval of 168 hours.

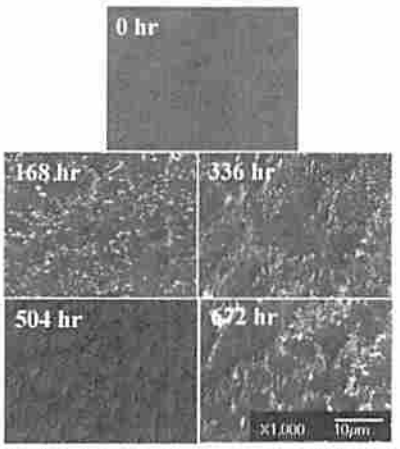

Figure 9: Optical Microscopic images of Phase Growth in CABGA36 at different time intervals at 125°C

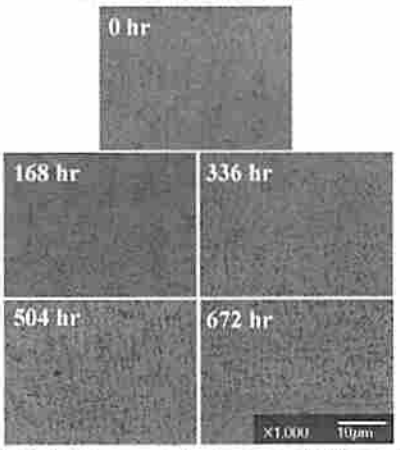

Figure 10: Optical Microscopic images of Phase Growth in CABGA256 at different time intervals at 125°C.

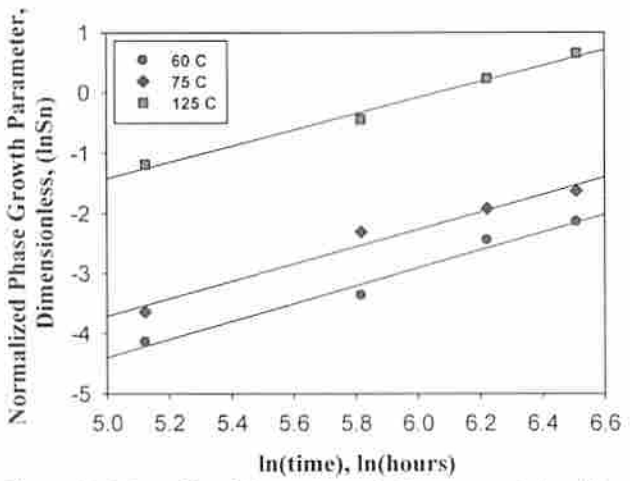

Figure 11: Normalized Phase Growth (S_n) versus Aging Time (t) for CABGA 36

The phase-coarsening in the microstructure is clearly visible by comparison of 672 hour microstructure with 0-hour microstructure. Figure 11 and Figure 12 show the plots of normalized phase growth at different isothermal aging temperature and at various time intervals for CABGA 36 and CABGA 256 respectively.

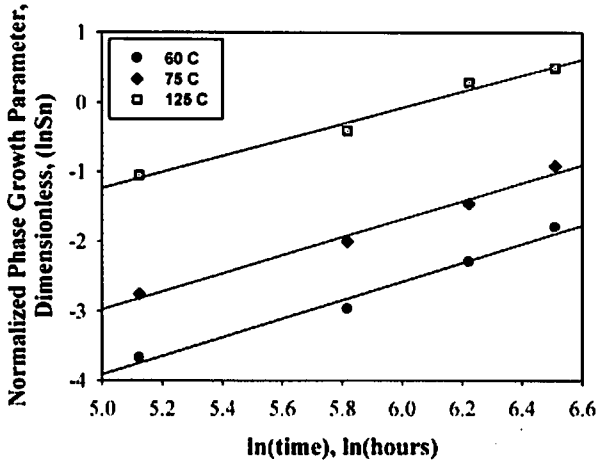

Figure 12: Normalized Phase Growth (S_n) versus Aging Time (t) for CABGA 256

Table 2: Normalized Phase Growth Coefficients and Exponents for the CABGA 36 Package

Temperature	Equation (3) $\ln(S_n)=\ln\left[\left(\frac{g_p}{g_0}\right)^4-1\right]=\ln a_0+b_0(\ln t)$	
	b_0	$\ln(a_0)$
60°C	1.488	-11.84
75°C	1.447	-10.95
125°C	1.337	-8.106

Table 3: Normalized Phase Growth Coefficients and Exponents for the CABGA 256 Package

Temperature	Equation (3) $\ln(S_n)=\ln\left[\left(\frac{g_p}{g_0}\right)^4-1\right]=\ln a_0+b_0(\ln t)$	
	b_0	$\ln(a_0)$
60°C	1.338	-10.60
75°C	1.293	-9.44
125°C	1.161	-7.04

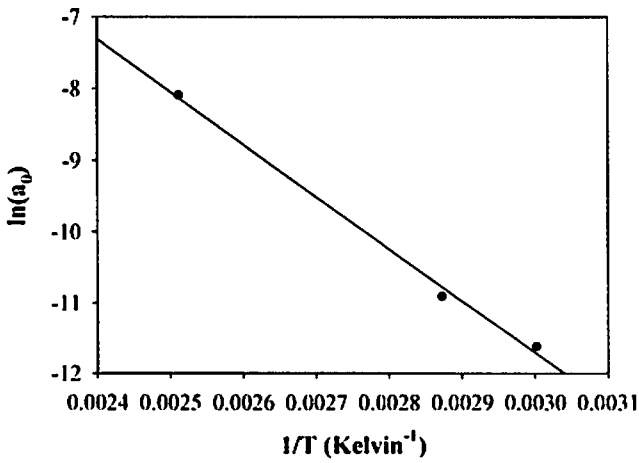

Figure 13: $\ln(a_0)$ versus Aging temperature for CABGA 36

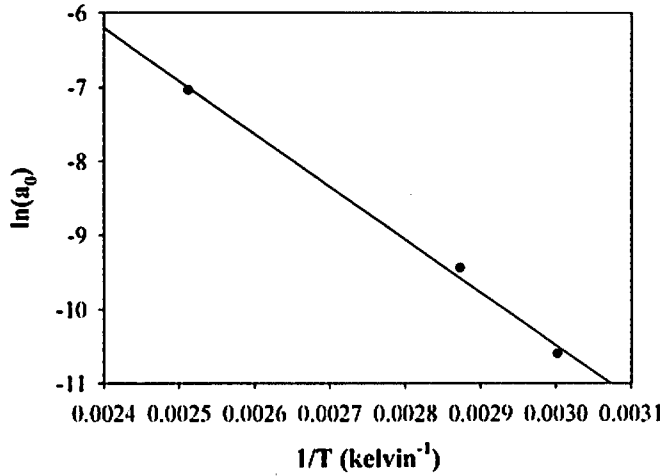

Figure 14: ln(a') versus Aging temperature for CABGA256

Table 4: Activation Energy for Phase Growth Coefficient

	$\ln(a_1)$	E_a (eV)
CABGA 36	10.268	0.63
CABGA 256	10.903	0.61

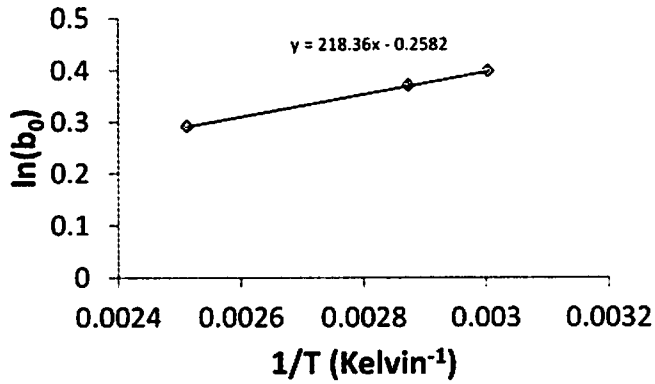

Figure 15: Plot of $\ln(b_0)$ and Aging temperature for CABGA36

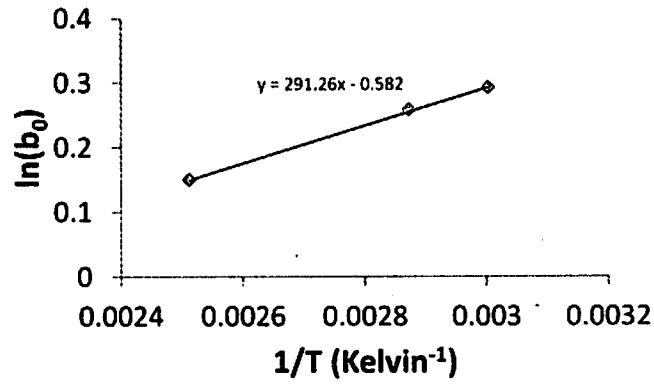

Figure 16: Plot of $\ln(b_0)$ and Aging temperature for CABGA256

The graphs for the higher temperature have higher normalized phase growth values. The increase in normalized phase growth parameter correlates with the underlying physics, since

the higher temperatures will produce more phase growth in an identical period of time. Equation (3) for phase growth evolution under thermal aging has been fit to experimental data. The equation parameters have been derived based statistical fit of the experimental data. Table 2 and Table 3 show the values for the phase growth coefficient and the phase growth exponent for the CABGA 36 and the CABGA 256 packages. Values indicate that the aging temperature increases the value of the phase growth coefficient. The coefficient term changes with temperature of exposure because of the underlying agglomeration of phases proceeds at a faster pace at a higher temperature. The activation energy of the coefficient term has been computed by fitting the data to Equation (7). Figure 13 and Figure 14 show the relationship between $\ln(a_0)$ and (1/T), where T is the absolute temperature. Slope of the fit of $\ln(a_1)$ versus (1/T) is E_A/K_B, where E_A is the activation energy; K_B is Boltzmann's Constant (8.617×10^{-5} ev/K). The Activation energy of phase growth is calculated as 0.63eV for CABGA 36 and 0.614eV for CABGA 256.

Table 5: Activation Energy for Phase Growth Exponent

	$\ln(b_1)$	E_B (eV)
CABGA 36	-0.258	0.019
CABGA 256	-0.582	0.025

Slope of this fit is E_B/K_B, where E_B is the activation energy; K_B is Boltzmann's Constant (8.617×10^{-5} ev/K). The Activation energy of phase growth is calculated as 0.019eV for CABGA 36 and 0.025eV for CABGA 256 (Table 5).

B. Intermetallic Thickness Damage Proxy

The image analysis software has been used to measure the average intermetallic thickness. Equation (10) has been used to capture the evolution of intermetallic growth under exposure to thermal aging. The data for normalized intermetallic thickness versus aging time has been fit to Equation (10). The coefficient and activation energy has been derived from statistical fit of experimental measurements of the intermetallic growth from cross-sections.

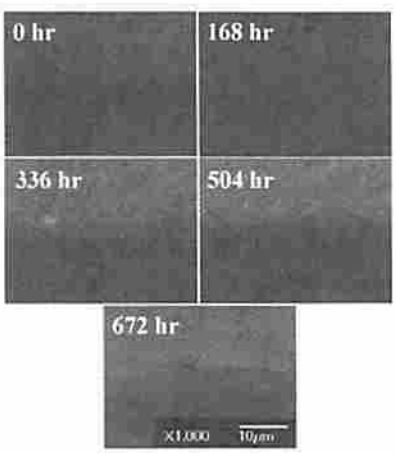

Figure 17: Optical Microscopic images of IMC Growth in CABGA36 at different time intervals at 60°C.

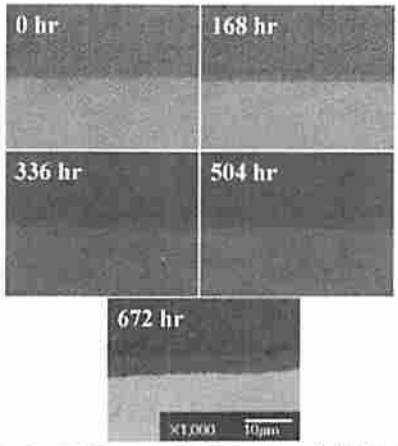

Figure 18: Optical Microscopic images of IMC Growth in CABGA256 at different time intervals at 60°C

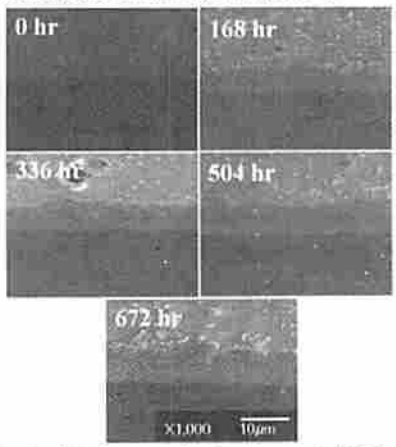

Figure 19: Optical Microscopic images of IMC Growth in CABGA36 at different time intervals at 75°C.

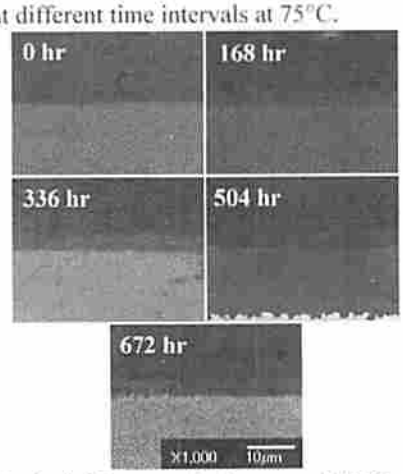

Figure 20: Optical Microscopic images of IMC Growth in CABGA256 at different time intervals at 75°C.

Micrographs of phase structure are shown in Figure 17, Figure 18 at 60°C, Figure 19, Figure 20 at 75°C, Figure 21 at 125°C for the CABGA 36 and CABGA 256 packages at a time-interval of 168 hours. The phase-coarsening in the microstructure is clearly visible by comparison of 672 hour microstructure with 0-hour microstructure.

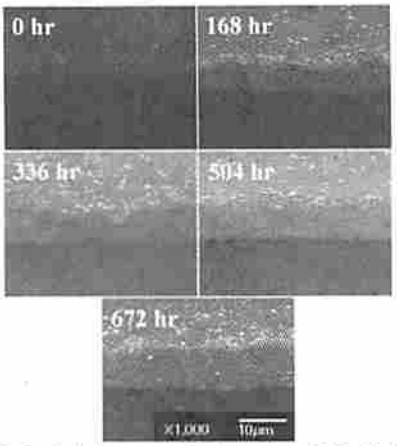

Figure 21: Optical Microscopic images of IMC Growth in CABGA36 at different time intervals at 125°C.

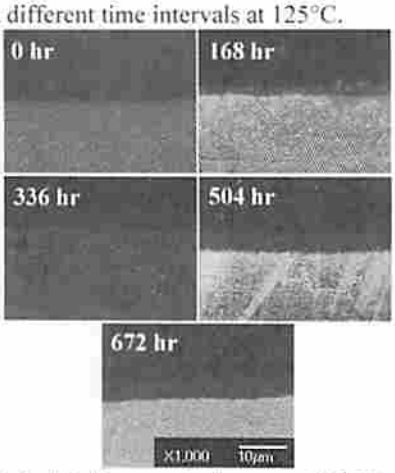

Figure 22: Optical Microscopic images of IMC Growth in CABGA256 at different time intervals at 125°C.

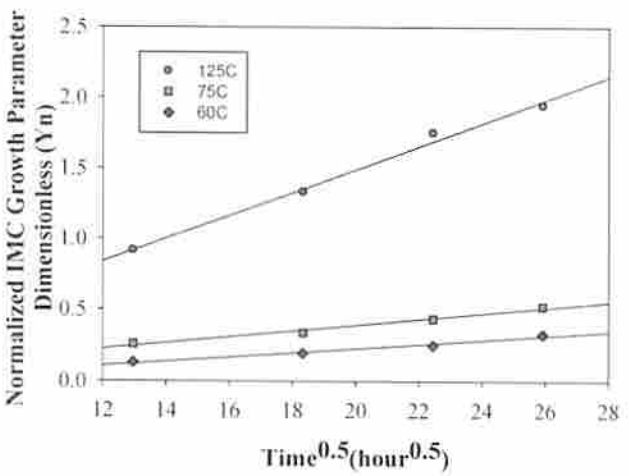

Figure 23: Relation between Normalized IMC Growth (Y_n) and Aging Time (t) for CABGA 36

Figure 23 and Figure 24 show the plots of normalized intermetallic growth at different isothermal aging temperature and at various time intervals for CABGA 36 and CABGA 256 respectively. The graphs for the higher temperature have higher normalized intermetallic growth values. The increase in normalized intermetallic thickness parameter correlates with the underlying physics, since the higher temperatures will produce more intermetallic thickness due to higher diffusion rates in an identical period of time. Equation (11) for IMC growth under thermal aging has been fit to experimental data. The equation parameters have been derived based statistical fit of the experimental data.

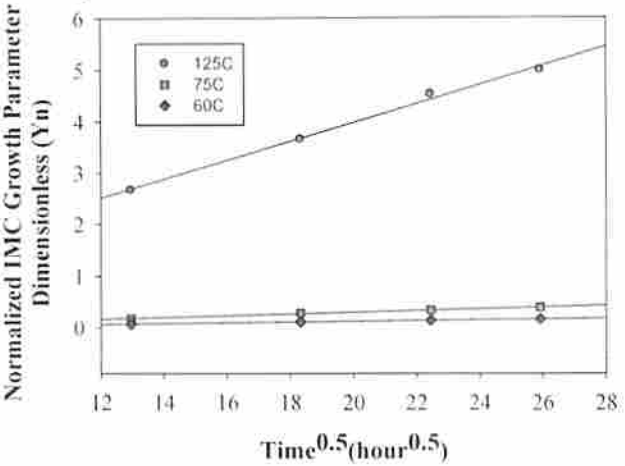

Figure 24: Relation between Normalized IMC Growth (Y_n) and Aging Time (t) for CABGA 256

Table 6: Normalized IMC Growth Coefficients and Exponents for the CABGA 36 Package

Temperature	Equation (10) $Y_n = k_t t^{0.5} \exp\left(\frac{-E_A}{K_B T}\right) = k_0 \sqrt{t}$	
	k_0 (CABGA36)	k_0 (CABGA256)
60°C	0.0072	0.0071
75°C	0.0194	0.0168
125°C	0.2620	0.1833

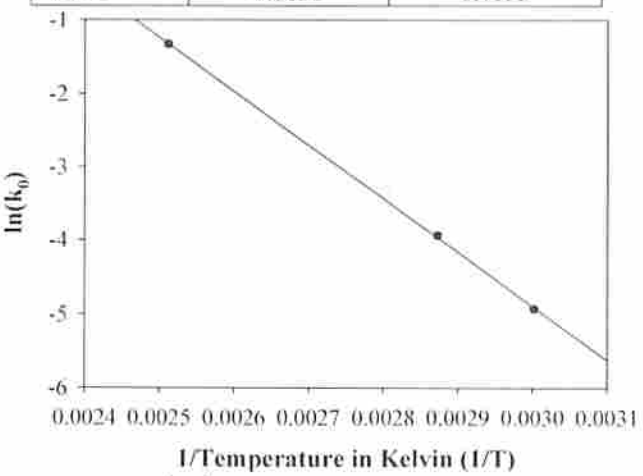

Figure 25: $\ln(k_0)$ vs Aging temperature for CABGA36

Table 6 shows the values for the IMC growth coefficient for the CABGA 36 and the CABGA 256 packages. Values indicate that the aging temperature increases the value of the IMC growth coefficient. The coefficient term changes with

temperature of exposure because of the underlying Fickian-diffusion at the interface proceeds at a faster pace at a higher temperature. The activation energy of the coefficient term has been computed by fitting the data to the following form of the Equation (13). Taking a natural logarithm of Equation (13), the relationship has been reduced to that of a straight line shown in Equation (14), where k_0 is the temperature dependent IMC-growth coefficient. Figure 25 and Figure 26 show the relationship between $\ln(k_0)$ and (1/T), where T is the absolute temperature.

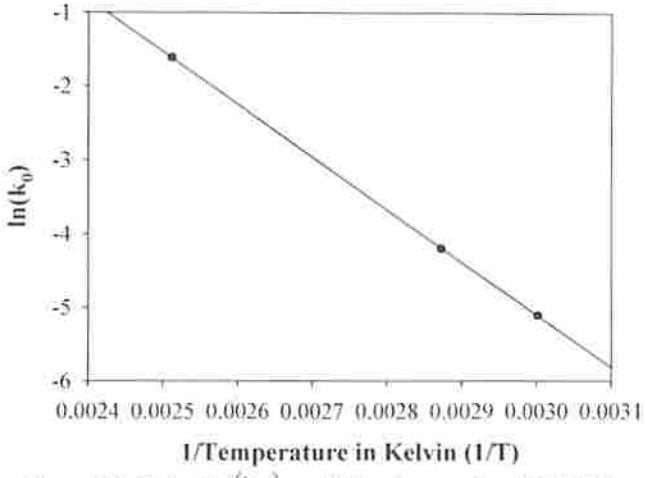

Figure 26: Plot of $\ln(k_0)$ vs Aging temperature (CABGA 256)

Table 7: Activation Energy for Phase Growth Coefficient

	$\ln(k_1)$	Ea (eV)
CABGA 36	17.017	0.63
CABGA 256	14.954	0.57

Slope of this fit is E_A/K_B, where E_A is the activation energy; K_B is Boltzmann's Constant (8.617×10^{-5} ev/K). The Activation energy of phase growth is calculated as 0.63eV for CABGA 36 and 0.57eV for CABGA 256.

V. Damage Mapping

In this section, a method for damage mapping has been developed using the data gathered on the test vehicles. Temperature and time combinations required to achieve a specified value of normalized phase growth have been calculated. The damage accrued can thus be sustained in a shorter time at a high temperature or in a longer time at a lower temperature. Re-arranging Equation (5),

$$\ln(S_n) = \ln(a_0) + b_0 \ln(t) \quad (15)$$

$$\ln(S_n) = \ln\left(a_1 \exp\left(\frac{-E_a}{KT}\right)\right) + b_1 \exp\left(\frac{-E_b}{KT}\right)\ln(t) \quad (16)$$

Re-arranging the equation: (17)

$$\ln(t) = \frac{\ln(S_n) - \ln(a_1) + \left(\frac{E_a}{K_B T}\right)}{b_1 \exp\left(\frac{E_b}{K_B T}\right)}$$

Where, K_B is the Boltzmann's constant, 8.617e-5 eV/K, a1 = 28796.23, E_a = 0.63 eV, b1 = 0.772, E_b = 0.019 eV. Figure 27 shows the relation between aging temperatures (1/T) in Kelvin scale and required aging time in hours for a particular value of damage state in terms of phase growth for both the CABGA 36 and CABGA 256 packages.

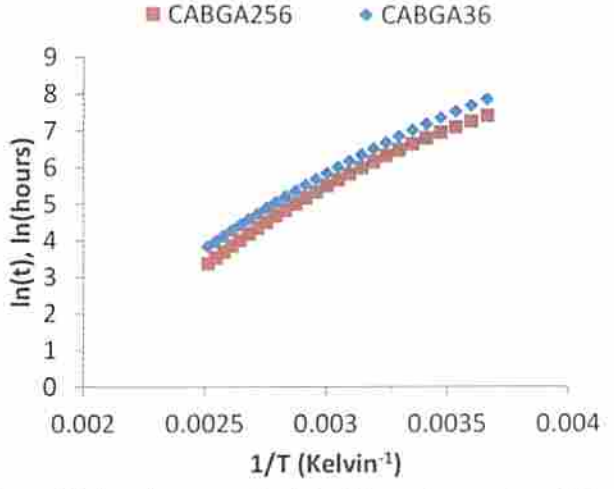

Figure 27: Iso-phase growth plots of Aging temperature (T) vs Aging time(t) for Phase Growth

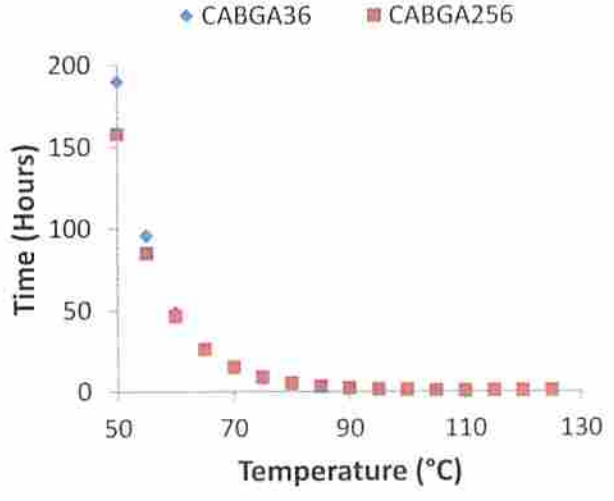

Figure 28: Iso-IMC growth plots of Aging Time, ln(T) vs Aging Temperature.

Convergence of damage mapping has been demonstrated by comparing the damage mapping data from two identical failure mechanisms for two different parts. Similarly, Figure 28 shows the same relations for IMC. In this section, a method for damage mapping has been developed using the data gathered on the test vehicles. Temperature and time combinations required to achieve a specified value of

normalized IMC growth have been calculated. The damage accrued can thus be sustained in a shorter time at a high temperature or in a longer time at a lower temperature. Re-arranging Equation (10).

$$t = \left(\frac{Y_n}{k_1 \exp\left(\frac{-E_A}{K_B T} \right)} \right)^2 \quad (18)$$

Where, K_B is the Boltzmann's constant, 8.617e-5 eV/K, k1 = 2.46e7. The convergence of the curves for the same failure mechanisms indicates the merit of the proposed approach.

VI. Using the Damage Mapping for Overlapping Environments

The 256 BGA test assemblies have been exposed to 168 hours of aging at 125°C, followed by 250 cycles in -40°C to 125°C (TC1) and then redeployed in thermal cycling environment of 0 to 100°C (TC2). The problem statement is to find the previous consumed life and the remaining useful life in TC2. In order to prognosticate the prior accrued damage and the remaining useful life, the parts have been withdrawn at periodic intervals of 250 cycles to measure the phase growth and intermetallic growth in the TC2 deployed samples. The withdrawn samples have been cross-sectioned.

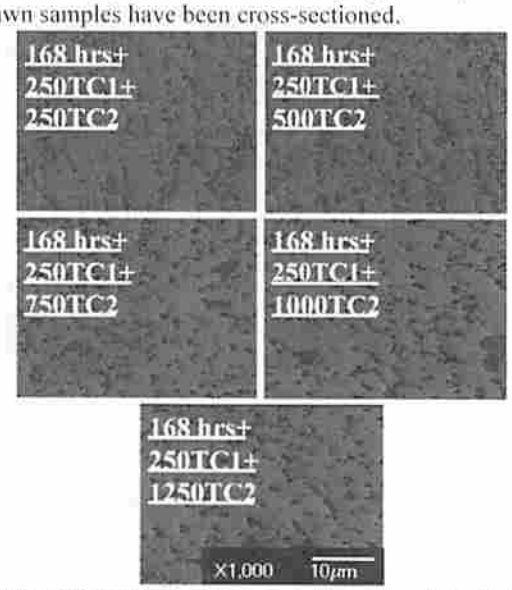

Figure 29: Optical Images for samples exposed to Multiple Environments of 168 hours @ 125°C + 250 Cycles TC-1 + x-Cycles TC-2, 256 I/O PBGA, magnification 1000x for Phase Growth.

The normalized phase growth parameter and normalized intermetallic thickness have been studied in the second-level interconnects of the test assemblies using a confocal microscope (Figure 29, Figure 30). Damage in the second-level interconnects of the test samples was prognosticated using the Levenberg-Marquardt Algorithm. Details of the LM algorithm can be found in [Madsen 2004]. Damage accrued from aging and cycling environments has been equivalenced based on two damage proxies including normalized intermetallic thickness and normalized phase growth. An identical measure of damage can be accrued in an electronic assembly using a varied combination of thermal stresses such as thermal aging and thermal cycling. Microstructural leading indicators have been used to identify the damage state and compute equivalent time under the future use conditions of the thermal aging and thermal cycling which will result in the same level of damage as sustained during environment conditions of prior deployment.

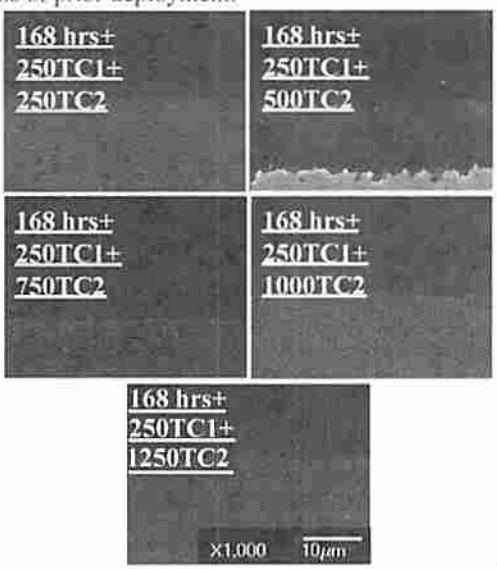

Figure 30: Optical Images for samples exposed to Multiple Environments of 168 hours @ 125°C + 250 Cycles TC-1 + x-Cycles TC-2, 256 I/O PBGA, magnification 1000x for IMC growth.

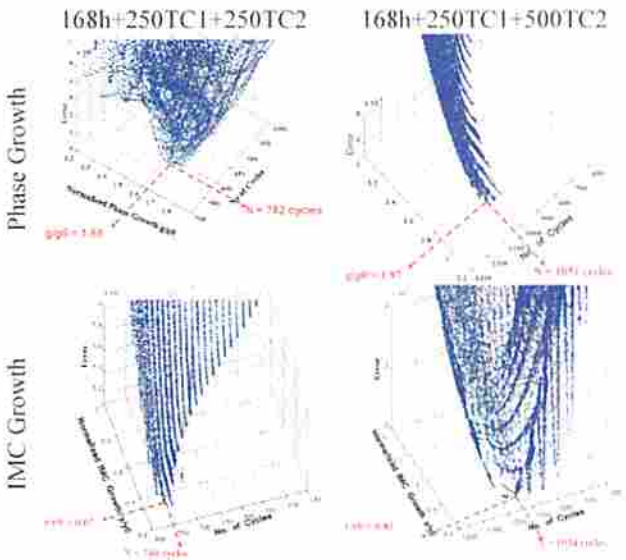

Figure 31: 3D plot of error versus Number of Cycles. Life computed from LM-algorithm for 168hrs TA + 250 cycles TC1 + 250 cycles TC2 and 168hrs TA + 250 cycles in TC1 + 500 cycles in TC2 for 256 PBGA.

The approach has been applied to both damage proxies of normalized phase growth and normalized intermetallic

thickness used in this study. Damage mapping relationships shown Equations (17) and (18) can be used to map damage to different storage temperature, e.g. if the test data was acquired for 168 hours at 125°C, and the intended use condition involved storage at 75°C, then an equivalent storage time to accrue identical damage could be determined. Figure 31 shows the prognosticated values of accrued damage in 256 BGA assemblies after they have been subjected to (a) 168 hours of thermal aging + 250 Cycles of thermal cycling in TC1 (-40°C to 125°C) + 250 cycles of thermal cycling in TC2 (0°C to 100°C) (b) 168 hours of thermal aging + 250 Cycles of thermal cycling in TC1 (-40°C to 125°C) + 500 cycles of thermal cycling in TC2 (0°C to 100°C). The accrued damage has been prognosticated using both phase growth parameter and the intermetallic growth. The prognosticated TC2 cycles for the 168h+250TC1+250TC2 case using phase growth and IMC growth are 782 cycles and 760 cycles respectively. The prognosticated TC2 cycles for the 168h+250TC1+500TC2 case using phase growth and IMC growth are 1051 cycles and 1034 cycles respectively.

VII. Prognostics Performance Metrics

In this paper two separate prognostication models based on two leading indicators of failure viz. phase-growth and inter-metallic compound growth of second level solder interconnects have been proposed and implemented for the life prediction of electronics. The sole purpose of evaluating various performance metrics was to relatively compare the two models and see which leading indicator of failure accurately predicts life. For this seven different performance metrics viz. accuracy, precision, Mean Squared Error (MSE), and Mean Absolute Percentage Error (MAPE), α-λ accuracy, relative accuracy (RA) and cumulative relative accuracy (CRA) have been computed to compare the two models.

A. Average Bias

Average bias method averages the error in predictions made at all subsequent times after prediction starts for the j^{th} UUT. The metric can be extended to average bias over all UUTs to establish overall bias [Saxena 2008a, b].

$$B_j = \frac{\sum_{i=P}^{EOP} \left\{\Delta^j(i)\right\}}{(EOP - P + 1)} \tag{19}$$

B. Sample Standard Deviation (S)

Sample standard deviation measures the dispersion/speed of the error with respect to the sample mean of the error. This metric is restricted to the assumption of normal distribution of the error. It is, therefore, recommended to carry out a visual inspection of error plots [Saxena 2008a, b].

$$S(i) = \sqrt{\frac{\sum_{i=1}^{n} \left(\Delta^j(i) - M\right)^2}{n-1}} \tag{20}$$

Where M is sample mean of the error

C. Mean squared error (MSE)

Mean squared error averages the square prediction error for multiple UUTs at the same prediction horizon. A derivative of MSE is root mean square error (RMSE) [Saxena 2008a, b].

$$MSE(i) = \frac{1}{L}\sum_{j=1}^{L} \Delta^j(i)^2 \tag{21}$$

D. Mean absolute percentage error (MAPE)

MAPE averages the absolute error in the predictions of multiple UUTs at the same prediction horizon. Instead of the mean, median can be used to compute Median absolute percentage error (MdAPE) in similar fashion [Saxena 2008a, b]:

$$MAPE(i) = \frac{1}{L}\sum_{j=1}^{L} \left| \frac{100\Delta^j(i)}{r_*^j(i)} \right| \tag{22}$$

E. α-λ accuracy

The α-λ curve has been plotted for both the models as shown in Figure 32 and Figure 33. It is a normalized plot of Remaining Useful Life (RUL) Vs Life which is compared against the ground truth and the error bounds.

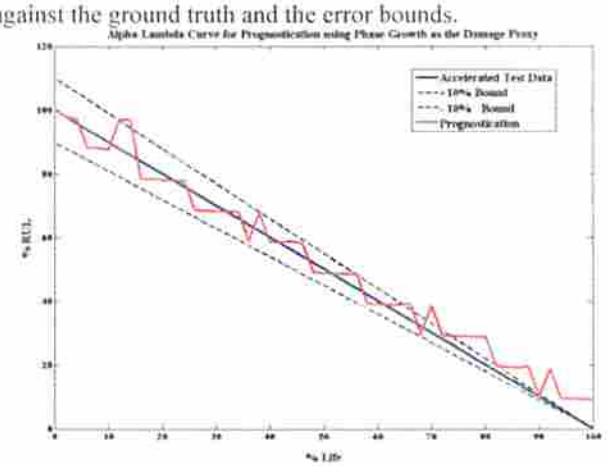

Figure 32: α-λ curve for Prognostication using phase-growth as the damage proxy

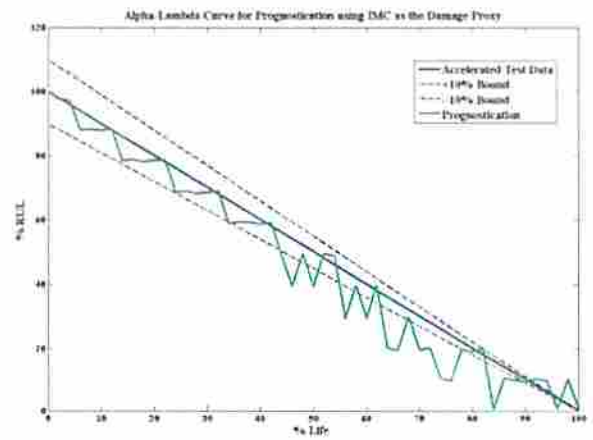

Figure 33: α-λ curve for Prognostication using IMC as the damage proxy

In this case the ground truth is the experimental data obtained from accelerated testing shown by blue line in the plots and ± 10% error bounds are imposed shown by dotted lines [Saxena 2008a, b]. It should be noted that the selection of error bounds is application specific and typically tighter bounds are imposed as the criticality of the system increases (Figure 32 and Figure 33).

F. Relative accuracy (RA)

Relative prediction accuracy is a notion similar to α-λ *accuracy* where, instead of finding out whether the predictions fall within a given accuracy levels at a given time instant, we measure the accuracy level. The time instant is again described as a fraction of actual remaining useful life from the point when the first prediction is made. An algorithm with higher relative accuracy is desirable [Saxena 2008a, b].

$$RA = 1 - \frac{\left| r_*(t_\lambda) - r'(t_\lambda) \right|}{r_*(t_\lambda)} \tag{23}$$

Where $t_\lambda = P + \lambda\,(EOP - P)$, where EOP is the end of the prediction, and P is the time index at which the first prediction is made.

G. Cumulative Relative Accuracy (CRA):

Relative accuracy can be evaluated at multiple time instances. To aggregate these accuracy levels, we define Cumulative Relative Accuracy as a normalized weighted sum of relative prediction accuracies at specific time instances [Saxena 2008a, b].

$$CRA = \frac{1}{EOP - P + 1} \sum_{1-P}^{EOL} RA \tag{24}$$

Where w is a weight factor as a function of RUL at all time indices. In most cases it is desirable to weigh the relative accuracies higher closer to the EOL.

Table 8: Comparison of Prognostics Metrics for the Two Leading Indicators

Prognostic Metrics	LM prognostication (Phase Growth)	LM prognostication (IMC)
Sample Standard Deviation (S)	220.6121	292.8947
MSE	54181.35	130216.3
MAPE	0.065839	0.177259
RA (λ=0.5)	0.9732	0.7836
CRA	0.007713	0.0074246

Table 8 shows the prognostics metrics for a point where 50% of the life of system is consumed. Both leading indicators based prognostic algorithms show comparable performance.

VIII. Summary and Conclusions

A damage mapping method has been developed based on the underlying physics-based leading indicators to relate the accrued damage under accelerated steady-state thermal storage to accrued damage under exposure to operational steady-state temperature. The method has been developed on two different board assemblies with two different packages including the CABGA36 and the CABGA26 packages. Analysis results indicate convergence of damage mapping relationships for the two package architecture examined for the failure mechanisms of solder joint failure and excessive intermetallics. The usefulness of the damage equivalency relationships has been demonstrated in the presence of overlapping thermal stresses.

IX. Discussion

It is true that many additional factors including surface finish, pad morphology (SMD, NSMD), board thickness, chip size, pad finish may influence the solder joint reliability. The focus of the current study is assessment of accrued damage in the assemblies. The influence of board thickness and chip size will influence the plastic work in the solder joints and thus be captured in the phase coarsening measurements in the present study. Localized effects in the solder joints such as those caused by surface finish, pad morphology and pad finish on the component and the board assembly will influence life of the joint through variation in the damage thresholds that cause failure. For example, the change in the finish may result in earlier failure due to higher propensity for crack initiation and propagation in certain finishes. Furthermore, the use of SMD may predispose the solder joint for earlier failure through the provision of a stress concentration at the edge of the solder mask – thus in the process lowering the damage threshold for crack initiation and progression. It is instructive to distinguish the damage pre-cursors and leading indicators of failure from the damage thresholds. Damage precursors used in the present study do not address the damage thresholds. Instead the damage precursors are intended for assessing the progression of damage in the solder joints and mapping of damage across a number of thermal operating and storage conditions. However, the driving mechanism for the accrual of damage, which is differential thermal mismatch in the solder joints may vary with the changes in the environmental conditions and some of the global geometry and architecture of the electronic assembly. It is this accrual of damage and mapping of damage which the leading indicators of damage target in the electronic assemblies.

Acknowledgment

The research results presented in this paper are based on projects supported by industrial members of the NSF-CAVE3 Electronics Research Center at Auburn University.

References

[1] Allen, D., Probabilities Associated with a Built-in-Test System, Focus on False Alarms, Proceedings of IEEE AUTOTESTCON, pp. 643-645, Sept 22-25, 2003.

[2] Anderson, N., and Wilcoxon, R., Framework for Prognostics of Electronic Systems, Proceedings of International Military and Aerospace Avionics COTS Conference, Seattle, WA, Aug 3-5, 2004.

[3] Chandramouli, R., Pateras, S., Testing Systems on a Chip, IEEE Spectrum, Vol. 33, No. 11, pp. 42-47, Nov. 1996.

[4] Chou, G. J. S., "Microstructure Evolution of SnPb and SnAgCu BGA Solder Joints During Thermal Aging," Proceedings of the 8th Symposium on Advanced Packaging Materials, pp. 39-46, 2002.

[5] Drees, R., and Young, N., Role of BIT in Support System Maintenance and Availability, IEEE A&E Systems Magazine, pp. 3-7, August 2004.
[6] Gao, R. X., Suryavanshi, A., BIT for Intelligent System Design and Condition Monitoring, IEEE Transactions on Instrumentation and Measurement, Vol. 51, Issue: 5, pp. 1061-1067, October 2002.
[7] Hasegawa, K., Noudou, T., Takahashi, A., and Nakaso, A., "Thermal Aging Reliability of Solder Ball Joint for Semiconductor Package Substrate," Proceedings of the 2001 SMTA International, pp.1-8, 2001.
[8] Hassan, A., Agarwal, V. K., Nadeau-Dostie, B., Rajski, J., BIST of PCB Interconnects Using Boundary- Scan Architecture, IEEE Transactions on Computer-Aided Design, Vol. 11, No. 10, pp. 1278-1288, October 1992.
[9] Jarrell, D., Sisk, D., Bond, L., Prognostics and Condition Based Maintenance (CBM) A Scientific Crystal Ball, Pacific Northwest National Laboratory, Richland, WA, International Congress on Advanced Nuclear Power Plants (ICAPP), paper number 194 June 2002.
[10] Lall, P., Islam, N., Suhling, J., Prognostication and Health Monitoring of Leaded and Lead Free Electronic and MEMS Packages in Harsh Environments, Proceedings of the 55th ECTC, pp. 1305-1313, Orlando, FL, 2005.
[11] Lall, P., Harsha, M., Kumar, K., Goebel, K., Jones, J., Suhling, J., Interrogation of Accrued Damage and Remaining Life in Field-Deployed Electronics Subjected to Multiple Thermal Environments of Thermal Aging and Thermal Cycling, Proceedings of the 61st ECTC, pp.775-789, 2011.
[12] Lall, P., Lowe, R., Goebel, K., Keynote Presentation: Prognostics and Health Monitoring of Electronic Systems, IEEE 12th. Int. Conf. on Thermal, Mechanical and Multiphysics Simulation and Experiments in Microelectronics and Microsystems, EuroSimE, Linz, Austria, pp. 1-17, 2011.
[13] Lall, P., Harsha, M., Suhling, J., Goebel, K., Sustained Damage and Remaining Useful Life Assessment in Leadfree Electronics Subjected to Sequential Multiple Thermal Environments, Proceedings of the 62nd ECTC, pp.1695-1708, May 29-June 1, 2012.
[14] Lall, P., Lowe, R., Goebel, K., Prognostication of Accrued Damage in Board Assemblies Under Thermal and Mechanical Stresses, Proceedings of the 62nd ECTC, pp.1475 - 1487, May 29-June 1, 2012.
[15] Lourakis, M., I., A., A brief Description of the Levenberg- Marquardt algorithm implemented by Levmar, Foundation of Research and Technology – Hellas (Forth), Greece, pp. 1- 6, Feb 11, 2005.
[16] McCann, R. S., L. Spirkovska, Human Factors of Integrated Systems Health Management on Next-Generation Spacecraft, First International Forum on Integrated System Health Engineering and Management in Aerospace, Napa, CA, pp. 1-18, November 7-10, 2005.
[17] Madsen, K., Nielsen, H., B., Tingleff, O., Methods for Non- Linear Least Squares Problems, Technical University of Denmark, Lecture notes, available at http://www.imm.dtu.dk/courses/02611/nllsq.pdf, 2nd Edition, pp. 1-30, 2004.
[18] Marko, K.A., J.V. James, T.M. Feldkamp, C.V. Puskorius, J.A. Feldkamp, and D. Roller, Applications of Neural Networks to the Construction of "Virtual" Sensors and Model-Based Diagnostics, Proceedings of ISATA 29th International Symposium on Automotive Technology and Automation, pp.133-138, June 3-6, 1996.
[19] Mishra, S., Pecht, M., In-situ Sensors for Product Reliability Monitoring, Proceedings of SPIE, vol. 4755, pp. 10-19, 2002.
[20] Nielsen, H., B, Damping Parameter in Marquardt's Method, Technical Report. IMM-REP-1999-05, Technical University of Denmark, Available at http://www.imm.dtu.dk/~hbn, pp. 1-16, 1999.
[21] Rosenthal, D., and Wadell, B., Predicting and Eliminating Built-in Test False Alarms, IEEE Transactions on Reliability, Vol. 39, No 4, pp. 500-505, October 1990.
[22] Saxena, A., J. Celaya, B. Saha, S. Saha, and K. Goebel, Evaluating Algorithm Performance Metrics Tailored for Prognostics, IEEE Aerospace Conference, Big Sky, MT, pp. 1-11, March 2008a.
[23] Saxena, A., J. Celaya, E. Balaban, K. Goebel, B. Saha, S Saha, and M. Schwabacher, Metrics for Evaluating Performance of Prognostic Techniques, Intl. Conf. on Prognostics and Health Management, Denver, Colorado, pp. 1-17, October 2008b.
[24] Schauz, J. R., Wavelet Neural Networks for EEG Modeling and Classification, PhD Thesis, Georgia Institute of Technology, 1996.
[25] Shiroishi, J., Y. Li, S. Liang, T. Kurfess, and S. Danyluk, Bearing Condition Diagnostics via Vibration and Acoustic Emission Measurements, Mechanical Systems and Signal Processing, Vol 11, No 5, pp.693-705, Sept. 1997.
[26] Williams, T. W., Parker, K. P., Design for Testability- Survey, Proceedings of the IEEE, Vol. 71, No. 1, pp. 98- 112, January 1983.
[27] Zhang, Y., Cai, Z., Suhling, J., Lall, P., Bozack M., The Effects of SAC Alloy Composition on Aging Resistance and Reliability, 59th Electronic Component and Technology Conference, San Diego, CA, pp. 370 – 389, May 26-29, 2009.
[28] Zorian, Y., A Structured Testability Approach for Multi Chip Boards Based on BIST and Boundary Scan, IEEE Transactions on Components, Packaging, and Manufacturing Technology-Part B, Vol. 17, No. 3, pp. 283-290, August 1994.

BIOGRAPHIES

Pradeep Lall (M'93—SM'08—F'12) is the John and Anne MacFarlane Endowed Professor with the Department of Mechanical Engineering, Director of the Harsh Environment Node of NextFlex Manufacturing Institute and the Director of the NSF Center for Advanced Vehicle and Extreme Environment Electronics at Auburn University. He received the B.E. degree in mechanical engineering from the Delhi College of Engineering, Delhi, India, in 1988, the M.S. and Ph.D. degrees in mechanical engineering from the University of Maryland, College Park, in 1989 and 1993, respectively, and the M.B.A. degree from Kellogg School of Management, Northwestern University, Evanston, IL, in 2002.

He was previously with Motorola's Wireless Technology Center. He has published extensively in the area of electronic packaging with emphasis on modeling and predictive techniques. He is author and co-author of 2-books, 14 book chapters, and over 430 journal and conference papers in the field of electronic packaging with emphasis on design, modeling, and predictive techniques. Dr. Lall is Fellow of the IEEE, a Fellow of the ASME, and a Fellow of the Alabama Academy of Science.

Dr. Lall is the recipient of the Wright A. Gardner Award of the Alabama Academy of Science, IEEE Exceptional Technical Achievement Award, ASME's Applied Mechanics Award, SMTA's Member of Technical Distinction Award, Auburn University's Creative Research and Scholarship Award, SEC Faculty Achievement Award, Samuel Ginn College of Engineering Senior Faculty Research Award, Three-Motorola Outstanding Innovation Awards, Five-Motorola Engineering Awards, and Twenty Best-Paper Awards at national and international conferences. He holds three U.S. Patents. Dr. Lall has served in several distinguished roles at national and international level including serving as member of National Academies Committee on Electronic Vehicle Controls, Member of the IEEE Reliability Society AdCom, IEEE Reliability Society Representative on the IEEE-USA Government Relations Council for R&D Policy, Chair of Congress Steering Committee for the ASME Congress, Member of the technical committee of the European Simulation Conference EuroSIME, and Associate Editor for the IEEE Transactions on Components and Packaging Technologies. He is a Six-Sigma Black-Belt in Statistics. He is the founding faculty advisor for the SMTA student chapter at Auburn University, and a member of the editorial advisory board for SMTA Journal.

Kazi Mahmud Mirza received his B. Sc. In Mechanical Engineering from Bangladesh University of Engineering and Technology (BUET) in 2005 and MBA from Institute of Business Administration, University of Dhaka in 2008. Currently he is Pursuing his PhD in Mechanical Engineering at Auburn University. His research concentration is in the area of fatigue reliability of solder joint.

Mahendra Harsha received the B.E. degree in mechanical engineering from the Rajasthan University, Rajasthan, India, in 2006, and Ph.D. degree in mechanical engineering at the NSF Center for Advanced Vehicle and Extreme Environment Electronics, Auburn University in 2013, under the guidance of Prof. Pradeep Lall. He is a Senior Packaging Engineer with Skyworks Solutions. His research area includes prognostication of electronic assemblies in thermo-mechanical environments.

Kai Goebel received the degree of Diplom-Ingenieur from the Technische Universität München, Germany in 1990. He received the M.S. and Ph.D. from the University of California at Berkeley in 1993 and 1996, respectively. Dr. Goebel is a senior scientist at NASA Ames Research Center where he leads the Diagnostics & Prognostics groups in the Intelligent Systems Division. In addition, he directs the Prognostics Center of Excellence and he is the Associate Principal Investigator for Prognostics of NASA's Integrated Vehicle Health Management Program. He worked at General Electric's Corporate Research Center in Niskayuna, NY from 1997 to 2006 as a senior research scientist. He has carried out applied research in the areas of artificial intelligence, soft computing, and information fusion. His research interest lies in advancing these techniques for real time monitoring, diagnostics, and prognostics. He holds eleven patents and has published more than 150 papers in the area of systems health management.